

Real-time and non-invasive measurements of cell mechanical behaviour with optical coherence phase microscopy

D Gillies^{1,2}, W Gamal², A Downes², Y Reinwald³, Y Yang³, A El Haj³, P O Bagnaninchi^{1*}

¹MRC Scottish Centre for Regenerative Medicine, The University of Edinburgh, Edinburgh, UK

²Institute for Bioengineering, School of Engineering, The University of Edinburgh, Edinburgh, UK

³Institute for Science and Technology in Medicine, Keele University, Keele, UK

*Corresponding Author: Pierre.Bagnaninchi@ed.ac.uk

Abstract

Cell mechanical behaviour is increasingly recognised as a central biophysical parameter in cancer and stem cell research, and methods of investigating their mechanical behaviour are therefore needed.

We have developed a novel qualitative method based on quantitative phase imaging which is capable of investigating cell mechanical behaviour in real-time at cellular resolution using Optical Coherence Phase Microscopy (OCPM), and stimulating the cells non-invasively using hydrostatic pressure. The method was exemplified to distinguish between cells with distinct mechanical properties, and transient change induced by cytochalasin D.

We showed the potential of qualitative phase imaging to detect nanoscale intracellular displacement induced by varying hydrostatic pressure in microfluidic channels, reflecting cell mechanical behaviour. Further physical modelling is required to yield quantitative mechanical properties.

Keywords: optical coherence phase microscopy, mechanical behaviour, real-time monitoring, hydrostatic pressure, phase imaging

1. Introduction

There are more than fifteen cancer deaths per minute globally [1], with over 90% of cancer deaths caused by metastasis [2]. Metastasis is known to alter the mechanical behaviour of cells from the nanoscopic to macroscopic scales [3], with metastatic potential increasing as cell stiffness decreases [4 - 7], and nanoscale features of synthetic surfaces have been shown to influence cell behaviour [8].

Similarly, stem cells are vitally important in regenerative and therapeutic medicine due to their self-renewal and differentiation abilities. Mechanical stimuli have been shown to have a major role in regulating stem cell behaviour, with differentiation controlled by the stiffness of the substrate where stem cells attach, through a mechanosensitive process [9]. Therefore, there is a clear need to investigate the mechanical behaviour of cancer cells and stem cells as well as their response to various mechanical stimuli.

Clinicians have used manual palpation of suspect tissues as a qualitative diagnostic tool for centuries. It is, however, subjective, and carried out on the macroscopic scale. Non-invasive imaging techniques such as ultrasound and Magnetic Resonance Imaging (MRI) elastography have translated to the clinic [10, 11], however both lack the spatial resolution to be used on the cellular scale. The measurement of mechanical behaviour on the nano- and microscopic scale has used techniques such as atomic force microscopy (AFM), optical tweezers, and optical coherence elastography (OCE)

40 [12, 13]. These do, however, suffer from drawbacks for single cell characterisation in that they use
41 contact loading or are unable to assess cellular mechanics in a 3D microenvironment.

42 AFM is one of the most common techniques currently available to assess cell mechanics [14-16]. It
43 uses a cantilever and tip to determine quantitative cell mechanical properties, achieving high
44 resolution and mechanical sensitivity, but is inherently invasive, and as a surface-based technique it
45 cannot investigate intracellular mechanical properties or when cells are cultured in a 3D
46 environment.

47 OCT is a low-coherence interferometry based imaging technique which uses the optical scattering
48 properties of a sample in a manner analogous to ultrasound to create either a 2-D or 3-D image
49 which shows structural features at the micrometer scale [17-19]. OCE is an extension of OCT which
50 maps the mechanical properties of tissue by detecting the depth-resolved deformation produced as
51 a result of compression [13, 20-22]. OCE is comparable to palpation in that a force is applied to the
52 sample under investigation and the resulting displacement tracked [3]. To date, OCE systems
53 typically achieve a depth of focus of 0.5 – 3 mm and A-scan rate greater than 20 kHz [13, 22].

54 Quantitative phase imaging (QPI) is an optical microscopy technique [23, 24] which uses the phase
55 contrast of a sample to improve upon intrinsic contrast imaging. The shift in optical path length
56 (OPL) created by the sample is measured quantitatively at the nanometre scale. It is a powerful
57 label-free tool which has been used to investigate the biophysics of red blood cells [25, 26], cell
58 growth [27], and track microbial motility [28].

59 Combining OCT with high transverse resolution confocal microscopy results in optical coherence
60 microscopy (OCM), achieving sub-micron resolution imaging with high dynamic range and sensitivity,
61 allowing for 3D cellular imaging. OCM further extends to Optical Coherence Phase Microscopy
62 (OCPM), a quantitative phase imaging method, to measure the phase changes and cross-sectional
63 depth information from a sample. It is sensitive to sub-micrometer changes in OPL, and achieves
64 high spatial resolution. It is therefore an ideal candidate for monitoring displacements. OCPM has
65 been used to characterise nanoscale cellular dynamics in live cells [29], and has been shown to
66 measure cell viability based on intracellular optical fluctuations [30, 31].

67 In this study, we aimed to propose a method for the contact-less assessment of cell mechanical
68 behaviour in vitro that will allow further longitudinal studies without damaging the cells or
69 compromising cell culture sterility. Therefore, we described a novel method based on a standard
70 commercial OCT that can measure the relative cell mechanical response to hydrostatic pressure non-
71 invasively and in real-time. This method will be easily translatable to any Fourier-domain OCT and
72 with some modifications to most of the QPI methods.

73

74

75 2. Materials and Methods

76

77 2.1 Cell culture

78 Breast cancer cells (MCF-7) and mouse fibroblasts (3T3) were used in this study to provide two
79 lineages with distinct mechanical properties. Both were cultured in Dulbecco's Modified Eagle
80 Medium (DMEM) with 10% foetal bovine serum, 1% L-glutamine and 1% Penicillin-Streptomycin.
81 Cells were incubated at 37^oC and 5% CO₂ and were passaged every 3 days. Cells were dissociated

82 using trypsin-EDTA and transferred to microfluidic channels (microslide IV, Ibidi) 24 hours prior to
83 experimentation. We used adherent cells lines that attached to the bottom substrate of the
84 channels.

85

86 2.2 Hydrostatic Force

87 In this study, we modulated the hydrostatic pressure in microfluidic channels to induce a hydrostatic
88 force on adherent cells attaching at bottom surface of the channels to produce a non-contact force
89 similar to previous work [32]. In this work, we used controlled cyclic square wave pressure, instead
90 of a pressure column. We generated a change in hydrostatic pressure in the microfluidics channels
91 by altering the air pressure in a fluid container (falcon, 50mL), connected through a Tygon (Saint-
92 Gobain, France) tube to microfluidic channels (microslide IV, Ibidi).

93 In first approximation, we can consider the cells as half-spheres attached to an incompressible solid
94 substrate (see figure 1). Pressure and force are transmitted equally to all directions, and on figure 1
95 we will have equal forces on the right and left side of the cell, with no net horizontal hydrostatic
96 component. Whereas there will be a net vertical force, F_v , at the top of the cell proportional to the
97 projected area. For a cell of radius r , we have:

98

$$99 F_v = (\Delta P + \rho gh)(\pi r^2) + \rho g V_w \quad (1)$$

100

101 Where ΔP is the applied pressure change above the atmospheric pressure, ρ is the water density
102 (1000 kgm^{-3}), h the height of the water column, and g the gravitational acceleration (9.81 ms^{-2}). V_w is
103 the volume of water on top of the cell starting from the cell top. It can be written as the difference
104 between the cell volume and the volume of an imaginary rectangular box surrounding the cell.

$$105 V_w = 8r^3 - (4/6)\pi r^2 \quad (2)$$

106 Typically for a cell of radius $20 \mu\text{m}$ and $\Delta P=1000 \text{ N.m}^{-2}$ (10 mbar) we calculated a net vertical force of
107 $1.2 \mu\text{N}$. However the actual cross-sectional area of a cell is much lower as attachment to the
108 substrate is made through adhesion focal point. This could lead to acting net vertical force an order
109 of magnitude lower, i.e. in the nano-Newton range.

110 In this study, MCF-7 and 3T3 cells were exposed to cyclic mechanical stimuli in the form of square
111 wave hydrostatic pressure from a microfluidic pressure pump (AF1, Elveflow, France), inside a
112 microfluidic channel with pressure ranging from 1000 Nm^{-2} to 20000 Nm^{-2} with frequencies ranging
113 from 80-300 mHz. It was ensured that no air bubbles were present in the sample medium by
114 allowing a flow of media through the microchannel before sealing with a Luer lock plug (Elveflow,
115 France).

116

117 2.3 Optical coherence phase microscopy

118 *Experimental setup*

119 The OCPM system was based around a commercial Thorlabs Callisto optical coherence tomography
120 (OCT) system, as shown in figure 2. The superluminescent light source was centred at 930 nm with a
121 full width half maximum (FWHM) of 90 nm, with an axial resolution of 5um in water. The scanning

122 rate is 1.2KHz; which was order of magnitude lower than state of the art OCT used for OCE. The light
123 source was output to a FC/APC fibre, which is the guided with an F280APC-B collimating lens
124 (Thorlabs, NJ, USA). The light path is then directed by galvanometers which control the image
125 acquisition, and finally is coupled into the side port of a Leica DMIRE2 microscope. The system is
126 built in a common path configuration to improve the phase stability [33]. Using a beamsplitter
127 (Thorlabs, NJ, USA), the brightfield image of the sample was collected digitally using a CMOS camera
128 (Thorlabs, NJ, USA). A full list of components can be found in section 6.

129 The acquired spectra were then processed as described in figure 3. First, the average background
130 was removed, then the signal is resampled in k-space. The modulation of the spectra, collected at a
131 spatial location x_i, y_i , encodes the in-depth location (z_i) of the scattering particles, which are retrieved
132 by zero-padding of the signal and fast Fourier transform. This forms the A-scan at the location (x_i, y_i)
133 and the real part [35] of the complex signal is compressed on a log scale to give a depth-dependent
134 intensity profile; while the phase at each depth z_i of the OCT signal is retrieved from the argument.

135

136 2.4 Quantifying intracellular displacement due to cyclic hydroforce

137 A 4D data cube (256x256x512x96 in x, y, z, t pixels) was captured with an acquisition frequency of
138 1,200 A-scans, or (x, z) scans, per second to sample the varying phase over time. A quantitative
139 measurement of the change in phase was calculated as the differing phase between successive B-
140 scans. A quantitative measurement of the change in phase was calculated as the differing phase
141 between successive B-scans. Therefore, the phase was unwrapped along the time-dimension and
142 not spatially. This was implemented directly with the Matlab (Mathworks) function unwrap.

143 The phase difference was then converted into displacement, d , through the following equation:

$$144 \quad d = \frac{\Delta\Phi\lambda_0}{4\pi n} \quad (3)$$

145 Where; n is the refractive index, λ_0 is the central wavelength and $\Delta\Phi$ is the phase difference
146 between adjacent B scans. In OCPM, the phase stability is defined as the square root of the phase
147 variance, which is inversely related to the SNR [34]. With a theoretical SNR of 83 db in air, the system
148 had a theoretical phase stability of 7×10^{-5} Radians[34]. In liquid medium, the SNR was measured as
149 35 dB corresponding to a phase resolution of 0.01 radian [34].

150 For rectangular input pressure, the relative displacement of each pixel, Δd , was then determined
151 through the equation:

$$152 \quad \Delta d = 2 * \Delta\Phi \text{ RMS}(x, y) \frac{\lambda_0}{4\pi n} \quad (4)$$

153 Where; $\Delta\Phi \text{ RMS}(x, y)$ is the root mean squared (RMS) phase change at each pixel as a result of the
154 induced displacement. This gives us a qualitative measurement of the cell mechanical behaviour in
155 response to hydrostatic pressure.

156 Our experimental set-up achieves a scan rate adequate for acquiring the mechanical behaviour of
157 cultured cells. Whilst the scan rate used in our system is lower than the current state of the art, this
158 method is easily translatable to *other systems* where a higher rate could be used.

159 2.5 Assessing whole cell response

160

161 To assess the whole cell mechanical qualitative behaviour we plotted the distribution of the root
 162 mean squared phase for all pixels within the cell, and analysed their distribution. Pixels belonging to
 163 a cell were determined by first, manually removing the first strong reflections associated with the
 164 plastic substrate, and then using an intensity-based mask to delineate the cells.

165

166 2.5 Cellscale Microsquisher®

167 In order to confirm an appropriate optical phantom for the OCPM set-up, 6% (w/v) agarose beads
 168 (Agarose bead technology, Madrid, Spain) of diameter 150 µm to 350 µm were subjected to parallel
 169 plate compression in a water bath at a strain rate of 2.5 µms⁻¹ using the Cell Scale Microsquisher®
 170 and results recorded in the associated Squisherjoy software. A 1 mm compression plate was
 171 attached to a 235 µm microbeam. The force vs displacement data was then converted into stress vs
 172 strain data, with the associated curve used to obtain a linear regression line from which the elasticity
 173 was calculated at 10% nominal compression of the sphere.

174 *Theory*

175 Force vs displacement data was converted to stress vs strain using a modified Hertz model [36] as
 176 described below.

$$177 \quad \Phi = \cos^{-1}\left(\frac{R-\delta}{R}\right) \quad (5)$$

$$178 \quad a = (R - \delta)\tan\Phi \quad (6)$$

$$179 \quad f(a) = \frac{2(1+\nu)R^2}{(a^2+4R^2)^{3/2}} + \frac{1-\nu^2}{(a^2+4R^2)^{1/2}} \quad (7)$$

$$180 \quad E = \frac{3(1-\nu^2)F}{4\delta a} - \frac{f(a)F}{\pi\delta} \quad (8)$$

181 Where; F is the applied force, R is the sphere radius, δ is the displacement, ν the Poisson's ratio (0.5)
 182 and E the Young's Modulus.

183

184 3. Results and Discussion

185 In this paper, we presented an optical coherence elastography method in which the novelty relied
 186 mostly on the way the mechanical forces were realised in a non-contact way to allow live cell
 187 measurement, and on the associated signal processing techniques. We demonstrated, and
 188 exemplified for single pixels in figure 7, that this method created intracellular displacements within
 189 the cells that were directly coupled to the input mechanical stimuli, and that they were correlated to
 190 transient changes in cell mechanical properties after addition of cytochalasin D, and that they could
 191 distinguish two exemplar cell line extensively studied for their mechanical properties. The proposed
 192 optical set-up was based on a commercial OCT engine (Callisto, Thorlabs) with relatively low
 193 specification when compared to recent advances in the field [], and could therefore translated easily
 194 to higher specifications OCT systems and with some small modification to most of the QPI
 195 techniques.

196 Figure 5 (a) shows the stress-strain curve of 6% agarose beads (Agarose bead technology, Madrid,
 197 Spain) acquired from plate to plate compression tests using the Cell Scale Microsquisher system,
 198 shown in (b). This was converted from force-displacement to stress strain using the modified Hertz

199 model described in section 2.5. The mean Young's modulus was determined to be $834 \text{ Pa} \pm 45 \text{ Pa}$ at
200 10% nominal compression of the bead. Single beads of varying diameter from 150-350 μm were
201 tested in a water bath. This helped us to confirm that the mechanical properties of agarose beads
202 were in the same order of magnitude as of biological cells that typically range in the 1 kPa region [5].
203 They were therefore a well calibrated test sample to test the new methods based on OCPM.

204 In figure 6 we report the mean intensity map (a) and phase response (b)-(d) of agarose beads of size
205 150-350 μm , measured using the novel OCPM system. The period of a 100 mbar hydrostatic
206 pressure was varied, with the phase response to 4 s, 6 s, and 12 s cycles shown in figure 6 (b), (c),
207 and (d) respectively at one pixel of the bead. The change in the time varying phase response
208 correlated directly to the change in pressure cycle. This demonstrated that OCPM could monitor
209 nanoscale displacements induced by hydrostatic pressure in materials with mechanical properties
210 comparable to biological cells; and could therefore be used to map the relative mechanical
211 properties of cells in a non-invasive and real-time manner.

212 We then used the OCPM system to measure the mechanical behaviour of MCF-7 cells in response to
213 varying hydrostatic pressure (figure 7), where we plot the response of a single pixel of the cell under
214 test. Here we show a bright field image of the MCF-7 cells in (a) with the corresponding OCPM en-
215 face image and OCPM B-scan or 'cell profile' in figure 7 (b) and (c). Cyclic stress was successfully
216 applied directly to cells within the microfluidic chip and the corresponding displacement was
217 recorded in real-time at the nanometre scale for each pixel of the cell (see figure 7 (d)-(k)). A change
218 in amplitude and/or frequency of the stimuli was translated to a corresponding cell response. In (d),
219 (e) and (f) the amplitude was varied, with the phase response of a single pixel within the cell to 0,
220 100, and 200mbar cycles of 6s shown respectively. Here we see a clear change in the phase response
221 which is directly proportional to the change in stimulus. Intra-cellular variability gives rise to some
222 variation in the amplitude of the response, however the proportional correspondence of the
223 response cycle to the hydrostatic pressure cycle is clear.

224 In (g), (h) and (i) we show the phase response to a variation in the period of the cyclic stress. The
225 response to 4, 6, and 12s cycles at an amplitude of 200mbar are shown here. Again, we can see that
226 the response clearly correlates to the change in stimulus.

227 We then looked at the ability of the system to monitor the relative biomechanical properties of cells
228 known to be of different stiffness. In (j) we show the phase response of MCF-7 cells to 50mbar of
229 pressure with a 6s period. We then exposed the cells to 10 μM cytochalasin-D, an actin polymerisation
230 inhibitor known to reduce cell stiffness [37], for 180 minutes prior to recording the phase response
231 in (k). We can see an increased response here, indicating that the cells were indeed softer after the
232 addition of Cytochalasin-D. We then calculated the mean RMS of the phase signal in (l) for all pixels
233 of the cell. This gives a quantitative comparison of the relative cell response which confirms that the
234 cells were indeed significantly softer as expected after exposure to the drug ($p < 0.01$), demonstrating
235 the potential of OCPM combined with hydrostatic pressure to monitor non-destructively and in real-
236 time cell mechanical behaviour.

237 In figure 8 we compare two cell lines with distinctly different mechanical properties. We compare
238 the properties of 3T3 cells with MCF-7 cells. 3T3 cells have previously been described as stiffer than
239 MCF-7 in [4]. In (a) we show an en-face image of MCF-7 cells, and of 3T3 in (d). Interferences
240 between the reflections from the cell membrane and the glass surface generates "spatial" coherent
241 interference fringes in intensity when the cell thickness is below the coherence gate ($< 5\mu\text{m}$ in this
242 case), hence the banding effect observed in (d). These fringes were however not detrimental to our
243 method as phase differences were calculated along the time dimension (successive B scans), and not

244 adjacent pixels. We show B-scans, or 'cell profiles' of MCF-7 and 3T3 in (b) and (e) respectively, and
245 the corresponding mechanical contrast maps of relative displacement in (c) and (f), where the
246 relative displacement increases as the map moves to yellow.

247 This map is quantified in (g) and (h) where we plot the relative displacement for all pixels in the cell
248 on a histogram. It is quite clear from this that the mean displacement of the MCF-7 cells is much
249 greater than that of the 3T3, showing a marked difference in the relative displacement between
250 different cell lines. The high level of mean displacement recorded for MCF-7 cells indicates a soft
251 cell, with the low mean displacement if 3T3 indicating a stiffer cell. This data agrees with the figures
252 previously reported in literature, which state that 3T3 cells are stiffer [38, 4].

253 This evidence indicates that this novel non-destructive method is capable of providing a qualitative
254 description of cell mechanical behaviour, and map of mechanical contrast. Qualitative mechanical
255 contrast has been shown as a clinically relevant method in [39-44].

256

257 4. Conclusions

258 We have described a new qualitative method, based on the principles of quantitative phase imaging,
259 to monitor in real-time and non-destructively the mechanical behaviour of cells in monolayers that is
260 directly translatable to the study of the mechanical behaviour of cancer cells and of the stem cell
261 niche. This method is also easily translatable to *in vivo* imaging.

262 We have monitored cell response to cyclic hydrostatic pressure. Nanoscale intracellular
263 displacements were recorded as a function of pressure and can be directly related to the
264 biomechanical properties of cells. Differences were observed in relative strain rates between the cell
265 lines under investigation. Further physical modelling will be required to yield quantitative
266 mechanical properties.

267

268 5 Acknowledgements

269 The authors are grateful to the research group of Dr Anthony Callanan in the Institute for
270 BioEngineering, University of Edinburgh, Edinburgh, UK for facilitating use of the Cell Scale
271 Microsquisher® system.

272 This work was supported by the School of Engineering, University of Edinburgh and the Engineering
273 and Physical Sciences Research Council and Medical Research Council [grant number EP/L016559/1],
274 and the UKRMP Engineering and exploiting the stem cell niche hub [grant number MR/K026666/1].

275 6 Supplier list

276

277 *Hydrostatic Pressure*

Hydrostatic pressure pump	AF1	Elveflow, France
Falcon tube medium accessory kit	50ml	Elveflow, France
Microfluidic channel	Microslide VI	Ibidi, Germany

278

279 *Optical Coherence Phase Microscopy*

OCT system	Callisto	Thorlabs, NJ, USA
Microscope	DMIRE2	Leica, Germany
2D Galvo system, silver coated mirrors	GVS002	Thorlabs, NJ, USA
2D Galvo system linear power supply	GPS011	Thorlabs, NJ, USA
30mm cage compatible smooth bore kinematic mount	KC1	Thorlabs, NJ, USA
F=50mm 1" mounted achromatic doublet, SM1 thread-mount, ARC: 650-1050nm	AC254-050-B-ML	Thorlabs, NJ, USA
30mm Cage cube-mounted non-polarizing beamsplitter, 700-1100nm, M4 Tap	CCM1-BS014/M	Thorlabs, NJ, USA
Fibre collimation package	F280APC-B	Thorlabs, NJ, USA
SM1 threaded adapter	AD11F	Thorlabs, NJ, USA

280

281 *Cellsacle Microsquisher*

Micro scale tension compression test system	Microsquisher	Cellsacle, ON, Canada
Microbeam cantilever	203.2nm	Cellsacle, ON, Canada
Compression plate	1mm x 1mm	Cellsacle, ON, Canada

282

283

284 7 References

- 285 [1] B. W. Stewart, C. P. Wild, World cancer report 2014, IARC Press, Lyon, 2014
- 286 [2] C. L. Chaffer, R. A. Weinberg, A perspective on cancer cell metastasis, *Science* 331(6024), 1559-
287 1564(2011)
- 288 [3] B. F. Kennedy, K. M. Kennedy, D. D. Sampson, A Review of Optical Coherence Elastography:
289 Fundamentals, Techniques, and Prospects, *IEEE J. Sel. Topics Quantum Electron.* 20(2), 272-
290 288(2014)
- 291 [4] J. Rother, H. Nöding, I. Mey, A. Janshoff, Atomic force microscopy-based microrheology reveals
292 significant differences in the viscoelastic response between malign and benign cell lines, *Open Biol.*
293 4(5), 140046(2014)
- 294 [5] M. Plodinec, M. Loparic, C. A. Monnier, E. C. Obermann, R. Zanetti-Dallenbach, P. Oertle, J. T.
295 Hyotyla, U. Aebi, M. Bentires-Alj, R. Y. H. Lim, C. Schoenberger, The nanomechanical signature of
296 breast cancer, *Nat. Nanotechnol.* 7(11), 757-756(2012)
- 297 [6] W. Xu, R. Mezencev, B. Kim, L. Wang, J. McDonald, T. Sulchek, Cell stiffness is a biomarker of the
298 metastatic potential of ovarian cancer cells, *PLoS One* 7(10), e46609(2012)
- 299 [7] Z. Zhou, C. Zheng, S. Li, X. Zhou, Z. Liu, Q. He, N. Zhang, A. Ngan, B. Tang, A. Wang, AFM
300 nanoindentation detection of the elastic modulus of tongue squamous carcinoma cells with different
301 metastatic potentials, *Nanomedicine* 9(7), 864-874(2013)
- 302 [8] E. K. F. Kim, E. M. Darling, K. Kulangara, F. Guilak, K. W. Leong, Nanophotography-induced
303 changes in focal adhesions, cytoskeletal organisation, and mechanical properties of human
304 mesenchymal stem cells, *Biomaterials* 31(6), 1299-1306(2010)
- 305 [9] A. J. Engler, S. Sen, H. L. Sweeney, D. E. Discher, Matrix elasticity directs stem cell lineage
306 specification, *Cell* 126(4), 677-89(2006)
- 307 [10] K. J. Glaser, A. Manduca, R. L. Ehman, Review of MR elastography applications and recent
308 developments, *J. Magn. Reson. Imaging* 36(4), 757-774(2012)
- 309 [11] R. M. S. Sigrist, J. Liau, A. E. Kaffas, M. C. Chammas, J. K. Willmann, Ultrasound elastography:
310 review of techniques and clinical applications, *Theranostics* 7(5), 1303-1329(2017)
- 311 [12] B. F. Kennedy, R. A. McLaughlin, K. M. Kennedy, A. C. Chin, A. Tien, B. Latham, C. B. Saunders, D.
312 D. Sampson, Optical coherence micro-elastography: mechanical-contrast imaging of tissue
313 microstructure, *Biomed. Opt. Express* 5(7), 2113-2124(2014)
- 314 [13] B. F. Kennedy, P. Wijesinghe, D. D. Sampson, The emergence of optical elastography in
315 biomedicine, *Nat. Photon* 11, 215-221(2017)
- 316 [14] G. Binnig, C. F. Quate, C. Gerber, Atomic force microscope, *Phys. Rev. Lett.* 56(9), 930-933(1986)
- 317 [15] M. Radmacher, R. W. Tillmann, M. Fritz, H. E. Gaub, From molecules to cells: imaging soft
318 samples with the atomic force microscope, *Science* 257(5078), 1900-1905(1992)
- 319 [16] D. Tsikritsis, S. Richmond, P. Stewart, A. Elfick, A. Downes, Label-free identification and
320 characterisation of living human primary and secondary tumour cells, *Analyst* 140(15), 5162-
321 5168(2015)

322 [17] D. Huang, E. A. Swanson, C. P. Lin, J. S. Schuman, W. G. Stinson, W. Chang, M. R. Hee, T. Flotte,
323 K. Gregory, C. A. Puliafito, J. G. Fujimoto, Optical Coherence Tomography, *Science* 254(5035), 1178-
324 1181(1991)

325 [18] P. H. Tomlins, R. K. Wang, Theory, developments and applications of optical coherence
326 tomography, *J. Phys. D: Appl. Phys.* 38(15), 2519(2005)

327 [19] A. M. Zysk, F. T. Nguyen, A. L. Oldenburg, D. L. Marks, S. A. Boppart, Optical coherence
328 tomography: a review of clinical development from bench to bedside, *J. Biomed. Opt.* 12(5),
329 051403(2007)

330 [20] J. M. Schmitt, OCT elastography: imaging microscopic deformation and strain of tissue, *Opt.*
331 *Express* 3(6), 199-211(1998)

332 [21] H. Ko, W. Tan, R. Stack, S. A. Boppart, Optical coherence elastography of engineered and
333 developing tissue, *J. Tissue Eng.* 12(1), 63-73(2006)

334 [22] A. Curatolo, M. Villiger, D. Lorenser, P. Wijesinghe, A. Fritz, B. Kennedy, D. D. Sampson,
335 Ultrahigh-resolution optical coherence elastography, *Opt. Lett.* 41(1), 21-21(2016)

336 [23] G. Popescu, Quantitative phase imaging of cells and tissues, McGraw-Hill, New York, 2012

337 [24] M. Mir, B. Bhaduri, R. Wang, R. Zhu, G. Popescu, Quantitative Phase Imaging, *Progress in Optics*
338 57, 133-217(2012)

339 [25] G. Popescu, Y. Park, W. Choi, R. R. Dasari, M. S. Feld, K. Badizadegan, Imaging red blood cell
340 dynamics by quantitative phase microscopy, *Blood Cell Mol. Dis.* 41(1), 10-16(2008)

341 [26] Y. Park, T. Yamauchi, W. Choi, R. Dasari, M. S. Feld, Spectroscopic phase microscopy for
342 quantifying hemoglobin concentrations in intact red blood cells, *Opt. Lett.* 34(23), 3668-3670(2009)

343 [27] K. Park, L. J. Millet, N. Kim, H. Li, X. Jin, G. Popescu, N. R. Aluru, K. J. Hsia, R. Bashir,
344 Measurement of adherent cell mass and growth, *Proc. Natl. Acad. Sci. USA* 107(48), 20691-
345 20696(2010)

346 [28] J. Kühn, B. Niraula, K. Liewer, J. K. Wallace, E. Serabyn, E. Graff, C. Lindensmith, J. Nadeau, A
347 Mach-Zender digital holographic microscope with sub-micrometer resolution for imaging and
348 tracking of marine micro-organisms, *Rev. Sci. Instrum.* 85(12), 123113(2014)

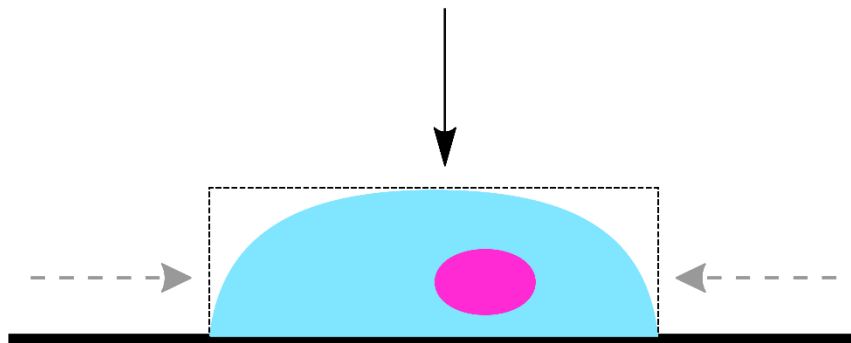
349 [29] A. K. Ellerbee, T. L. Creazzo, J. A. Izatt, Investigating nanoscale cellular dynamic with cross-
350 sectional spectral domain phase microscopy, *Opt. Express* 15(13), 8115-8124(2007)

351 [30] C. Holmes, M. Tabrizian, P. O. Bagnaninchi, Motility imaging via optical coherence phase
352 microscopy enables label-free monitoring of tissue growth and viability in 3D tissue-engineering
353 scaffolds, *J. Tissue Eng. Regen. Med.* 9(5), 641-645(2015)

354 [31] P.O. Bagnaninchi, C. Holmes, N. Drummond, J. Daoud, M. Tabrizian, Two-dimensional and three-
355 dimensional viability measurements of adult stem cells with optical coherence phase microscopy, *J.*
356 *Biomed. Opt.* 16(8), 086003(2011)

357 [32] L. A. G. Lin, A. Q. Liu, Y. F. Yu, C. Zhang, C. S. Lim, S. H. Ng, P. H. Yap, H. J. Gao, Cell
358 compressibility studies utilizing noncontact hydrostatic pressure measurements on single living cells
359 in a microchamber, *Appl. Phys. Lett.* 92(23), 233901(2008)

- 360 [33] K. S. Lee, H. Hur, H. Y. Sung, I. J. Kim, G. H. Kim, Spectrally encoded common-path fiber-optic-
361 based parallel optical coherence tomography, Opt. Lett 41(18), 4241-4244(2016)
- 362 **[34] Pierre phase stability [Bagnaninchi P, Journal biomedical optics, 2011]**
- 363 [35] M. V. Sarunic, B. E. Applegate, J. A. Izatt, Real-time quadrature projection complex conjugate
364 resolved Fourier domain optical coherence tomography, Opt. Lett. 31(16), 2426-2428(2006)
- 365 [36] K. Kim, J. Cheung, Q. Liu, X. Y. Wu, Y. Sun, Investigation of mechanical properties of soft
366 hydrogel microcapsules in relation to protein delivery using a MEMS force sensor, J. Biomed. Mater.
367 Res. 92(1), 103-113(2010)
- 368 [37] W. J. Elldridge, A. Sheinfeld, M. T. Rinehart, A. Wax, Imaging deformation of adherent cells due
369 to shear stress using quantitative phase imaging, Opt. Lett. 41(2), 352-355(2016)
- 370 [38] Y. M. Efremov, W. Wang, S. D. Hardy, R. L. Geahlen, A. Raman, Measuring nanoscale viscoelastic
371 parameters of cells directly from AFM force-displacement curves, Sci. Rep. 7, 1541(2017)
- 372 **[39] <https://link.springer.com/article/10.1186/s40644-016-0070-8>**
- 373 **[40] <https://www.ncbi.nlm.nih.gov/pmc/articles/PMC5108442/>**
- 374 **[41] <http://www.sciencedirect.com/science/article/pii/S0720048X15000248#!>**
- 375 **[42] <https://link.springer.com/article/10.1007/s12020-015-0654-2>**
- 376 **[43] <http://rsif.royalsocietypublishing.org/content/8/64/1521>**
- 377 **[44] <http://iopscience.iop.org/article/10.1088/0031-9155/58/4/923/meta>**



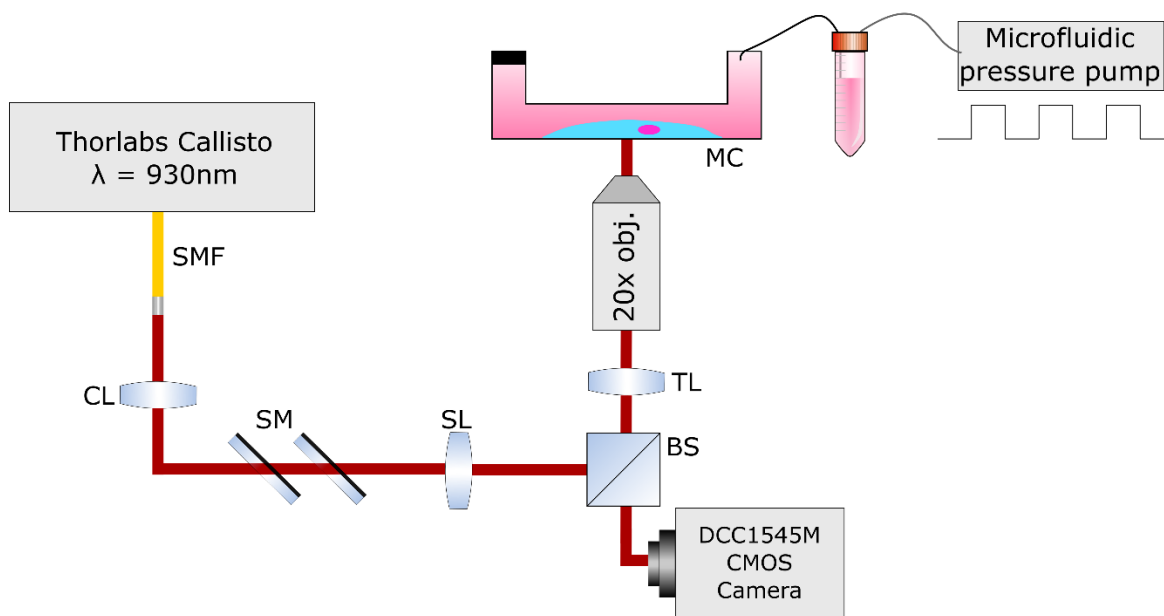
378

379

Figure 1: Resulting hydrostatic force induced on adherent cells above a substrate

380

381



382

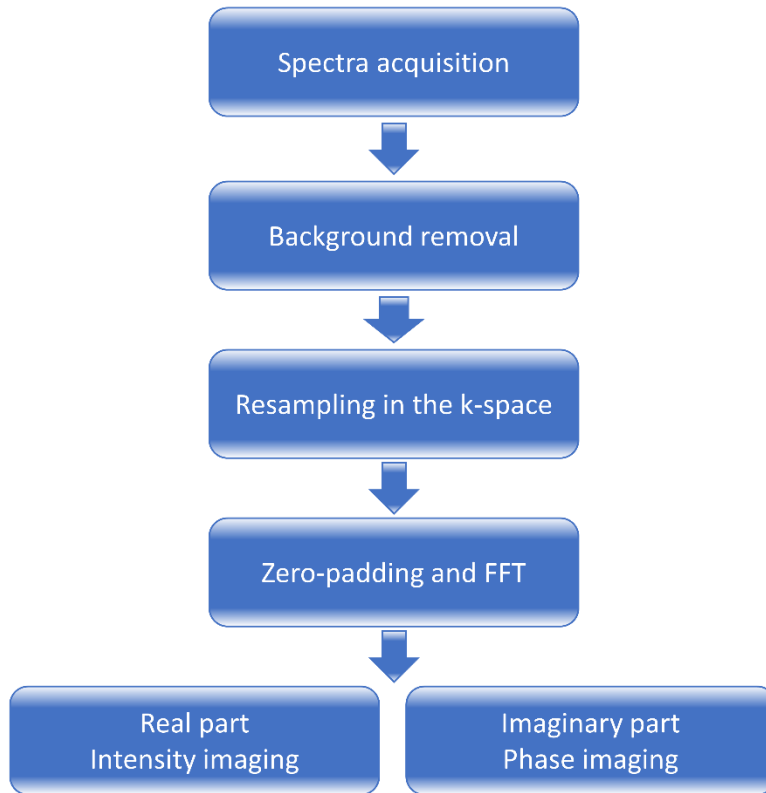
383

384 Figure 2: OCPM set-up for qualitative measurement of cell mechanical properties: SMF, single mode fibre; CL, collimating

385

lens; SM, scanning mirrors; SL, scanning lens; BS, beam splitter; TL, tube lens; MC, microchannel.

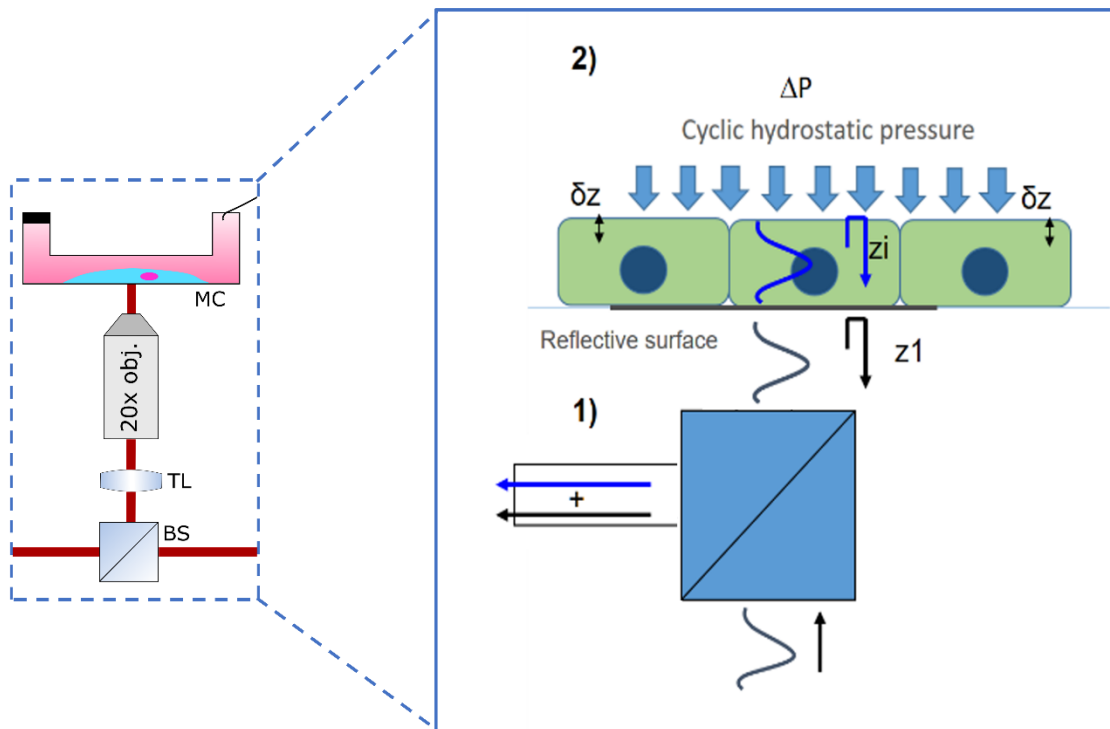
386



387

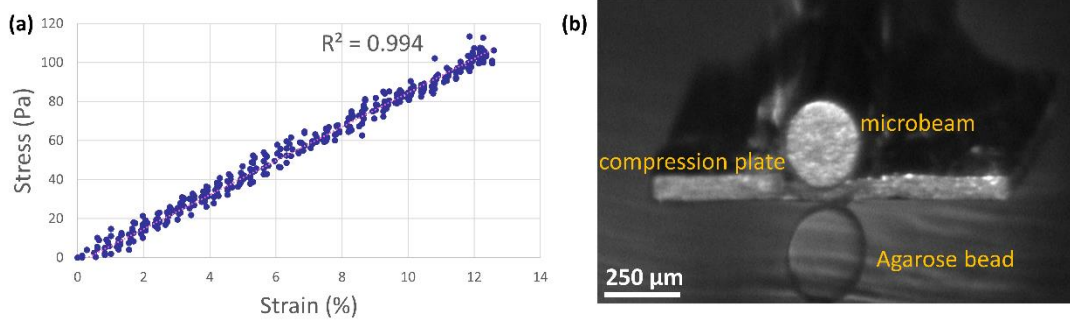
388 *Figure 3: Digital processing of acquired OCPM spectra to retrieve intensity image and phase information at each pixel.*

389



390

391 *Figure 4: Relative displacement induced by hydrostatic pressure measured as a change in phase. 1) Imaging system 2) Cyclic*
 392 *hydrostatic pressure is applied to cells which are cultured on a clear, reflective surface, which results in a change in the*
 393 *phase signal.*

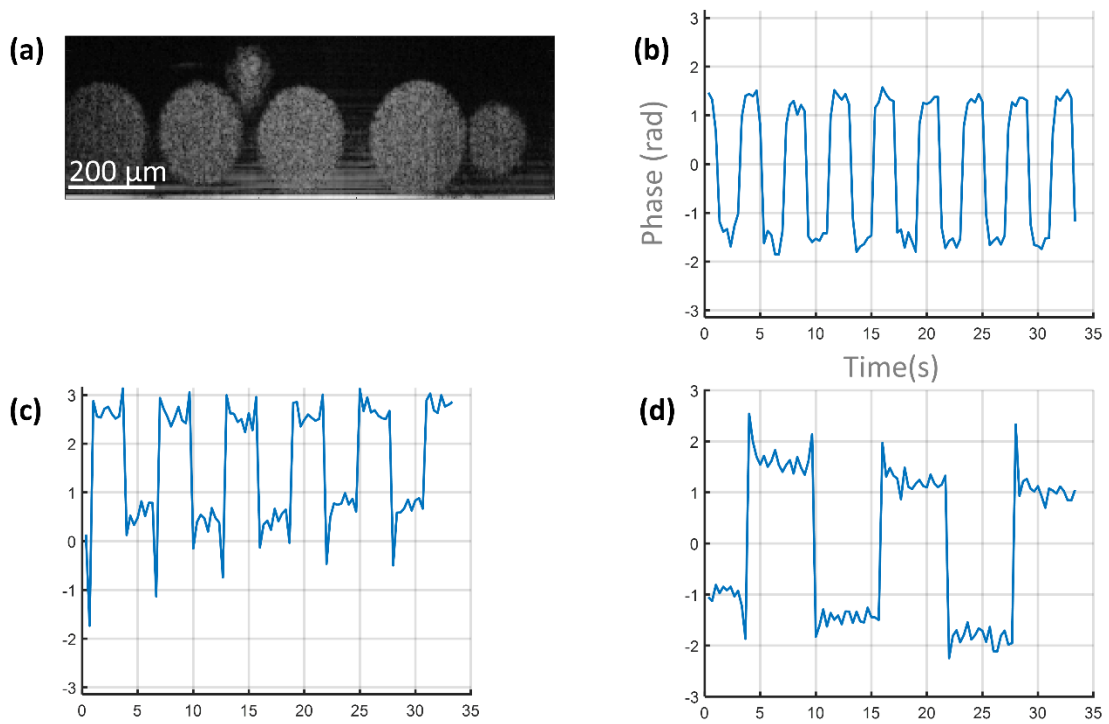


394

395

396

Figure 5: Mechanical properties of 6% agarose beads: Representative stress-strain curve of 350 μm bead (a), and compression testing in a water bath at strain rate of $2.5 \mu\text{ms}^{-1}$ (b).

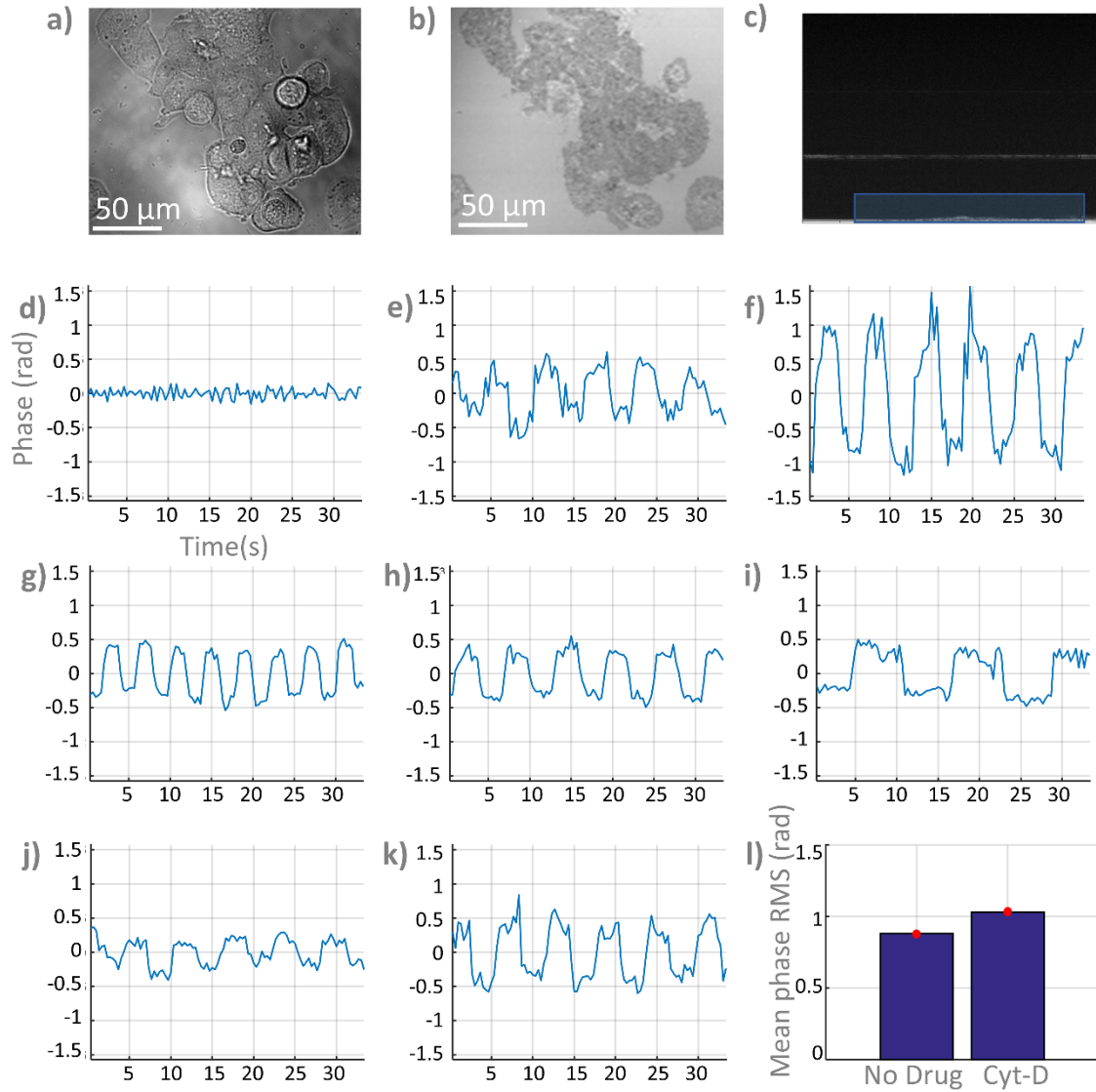


397

398

399

Figure 6: a) OCPM cross section of agarose beads, b-d) response to hydrostatic pressure of 4 s, 6 s, 12 s cycles with 100 mbar amplitude.



400

401

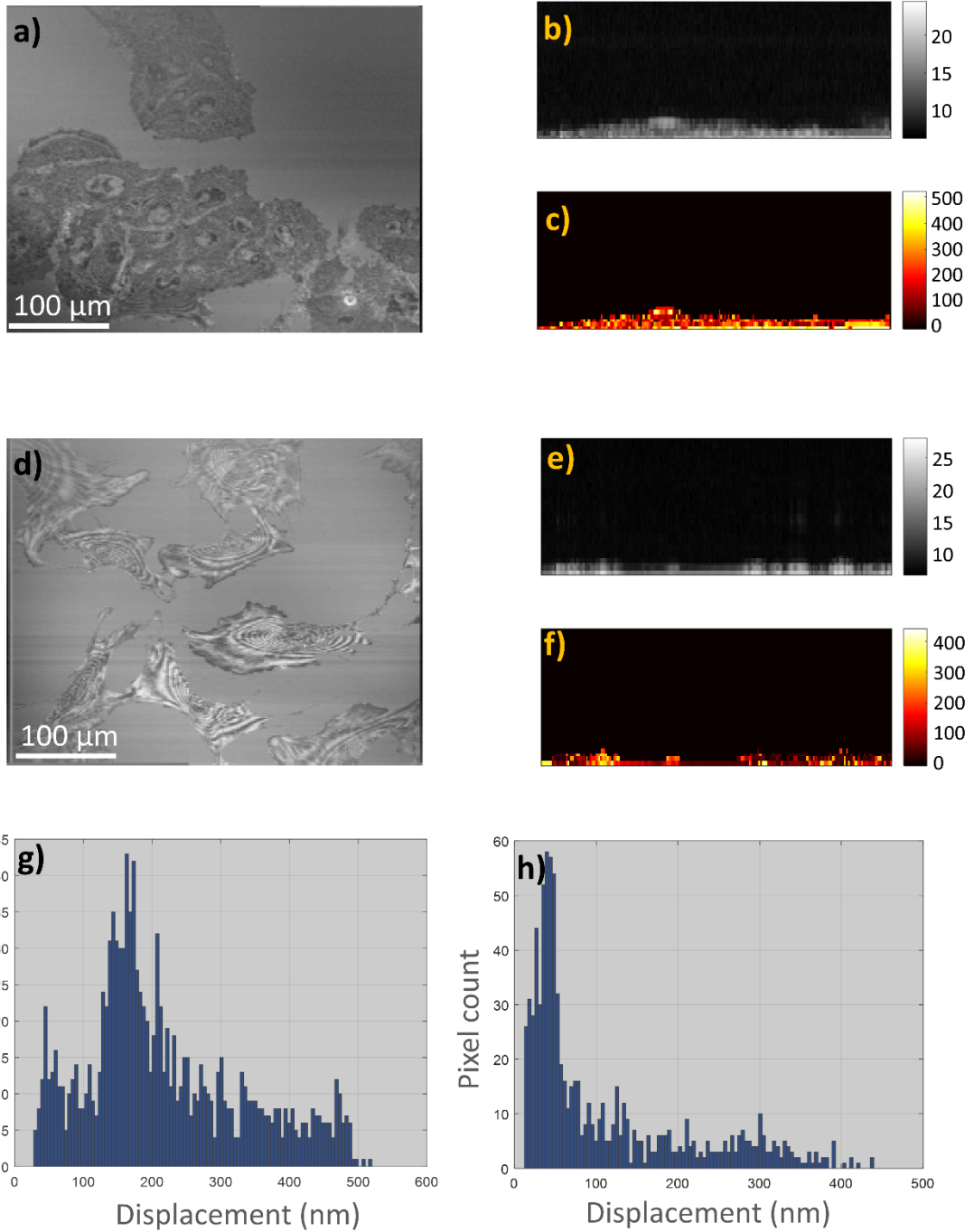
402

403

404

405

Figure 7: Bright field image (a), OCPM en-face (b), and OCPM 'cell profile' (c) of MCF-7 cells. Cell response at 0, 100, 200 mbar amplitude (d, e, f) with a 6 s cycle, and for various hydrostatic pressure period, 4 s, 6 s, 12 s cycles with 200 mbar amplitude (g, h, i), and (j) Typical cell response before drug addition (6 s, 50 mbar) and after addition of 10 μM Cytochalasin-D (k). (l) Mean response (N=242 pixels) shows significant ($p < 0.01$) increase in cell response. Phase value was taken at a representative pixel rather than the same pixel location within the cell.



406

407

408

409

410

411

Figure 8: OCPM en-face live imaging of MCF-7 cells (a) and 3T3 cells (d) with typical OCPM cross-section, 'cell profile', (b) and (e) and associated relative cell displacement induced by hydrostatic pressure (c) and (f). Heterogeneity in intracellular displacement was found in histograms of displacement (g, h) with a marked difference between 3T3 and MCF-7 which suggested 3T3 being stiffer.